Acta Materialia 162 (2019) 214–225

Contents lists available at ScienceDirect

Acta Materialia

journal homepage: www.elsevier.com/locate/actamat

Full length article

The formation mechanism of a novel interfacial phase with high thermal stability in a Mg-Gd-Y-Ag-Zr alloy

L.R. Xiao [a], Y. Cao [b], S. Li [b], H. Zhou [a, b, *], X.L. Ma [c], L. Mao [d], X.C. Sha [a], Q.D. Wang [e], Y.T. Zhu [b, c], X.D. Han [a, **]

[a] Beijing Key Lab of Microstructure and Property of Advanced Materials, Beijing University of Technology, Beijing, 100124, China
[b] Nano and Heterogeneous Material Center, School of Materials Science and Engineering, Nanjing University of Science and Technology, Nanjing, 210094, China
[c] Department of Materials Science & Engineering, North Carolina State University, Raleigh, NC, 27695, USA
[d] Shanghai Institute for Minimally Invasive Therapy, School of Medical Instrument and Food Engineering, University of Shanghai for Science and Technology, Shanghai, 200093, China
[e] National Engineering Research Center of Light Alloys Net Forming and State Key Laboratory of Metal Matrix Composite, Shanghai Jiao Tong University, 200240, Shanghai, China

ARTICLE INFO

Article history:
Received 15 August 2018
Received in revised form
21 September 2018
Accepted 3 October 2018
Available online 6 October 2018

Keywords:
Magnesium alloy
Grain boundary segregation
Interfacial phase
HAADF-STEM

ABSTRACT

Due to their unique precipitation behavior, magnesium-rare earth (Mg-RE) alloys exhibit excellent mechanical properties and decent thermal stability. In this work, a Mg-Gd-Y-Ag-Zr alloy was employed to investigate the segregation and interfacial phase formation at grain boundaries after plastic deformation and heat treatment. The interfacial phase was unequivocally investigated by aberration-corrected high-angle annular dark-filed scanning transmission electron microscopy (HAADF-STEM) from three different crystal directions and modeling, which reveals a hitherto unknown crystal structure (monoclinic: $\beta = 139.1°$, $a = 1.20$ nm, $b = 1.04$ nm and $c = 1.59$ nm). Its orientation relationship with the Mg matrix is: $[101]//[11\bar{2}0]_\alpha$, $[302]//[10\bar{1}0]_\alpha$ and $(010)//(0001)_\alpha$. Different from the precipitates in matrix, the size of the interfacial phase was not sensitive to annealing temperature between 250 °C and 400 °C. Transformation of twin boundaries to coaxial grain boundaries via multiple twinning led to the generation of many high strain sites along the boundaries, which promoted the formation of the interfacial phase. The interfacial phase was stable up to 400 °C, which was about 100 °C higher than the dissolution temperature of β′ and γ" precipitates.

1. Introduction

Mg and its alloys possess unique properties including high specific strength, good stiffness and excellent biocompatibility, which make them attractive for aerospace, automotives, electronics and biomedical applications [1–3]. Two of the major limiting factors for the application of Mg alloys are their comparatively low strength [4] and poor thermal stability [5]. In order to improve the strength of Mg alloys at both room and elevated temperatures, magnesium-rare earth (RE) alloys have been developed to improve age-hardening response and creep resistance [6,7].

Mg-Gd system alloys are a representative rare earth magnesium alloys, known for their outstanding mechanical properties. Homma et al. developed a Mg-Gd-Y-Zn-Zr alloy with an extraordinary high tensile strength of 542 MPa [8]. Nie et al. also reported that after age hardening the Mg-6Gd-2Zn-0.6Zr alloy could be made much stronger than Mg-Al, Mg-Zn and Mg-Mn alloys [9]. The outstanding mechanical properties of these Mg-RE alloys are mainly attributed to the formation of the rare earth precipitates, such as the peak aged β′ phase, which enhances the mechanical strength by blocking dislocation slip [10,11]. The thermal stability of the precipitates is much higher than that of grain boundaries (GBs), which helps with improving thermal stability [5,12]. Particularly, rare earth precipitates are stable at high temperatures if the content of the rare earth elements is sufficiently high [13], which makes them excellent for improving the high-temperature mechanical properties

* Corresponding author. Beijing Key Lab of Microstructure and Property of Advanced Materials, Beijing University of Technology, Beijing, 100124, China.
** Corresponding author.
E-mail addresses: hzhou511@njust.edu.cn (H. Zhou), xdhan@bjut.edu.cn (X.D. Han).

https://doi.org/10.1016/j.actamat.2018.10.005
1359-6454/

[14,15].

In conjunction with rare earth elements, addition of Ag has also been reported to significantly enhance the mechanical properties of Mg-RE alloys [16–19]. Zhang et al. produced a Mg-15.6Gd-1.8Ag-0.4Zr alloy with an outstanding ultimate tensile strength of ~423 MPa in the peak-aged condition [17]. It was also demonstrated that the Mg-Gd-Y-Ag alloy exhibits much higher yield strength than the Mg-Gd-Y alloy [18,19]. Recently, additional precipitation strengthening in Mg-Gd-Ag alloy was achieved by the formation of a unique basal plane phase, which coexists with β′ phase during aging treatment [20]. Zhu et al. reported that the basal plane phase in the Mg-6Y-2Ag-1Zn-0.6Zr alloy, named as γ", had an ordered hexagonal structure (P6/*mmm*, $a = 0.556$ nm, $c = 0.424$ nm), which is different from the long-period stacking ordered (LPSO) phase [21,22].

Although the strength of Mg alloys at both room and elevated temperatures can be improved significantly by age hardening, the ductility is usually sacrificed as a side effect. This is because the inter-precipitate distance is usually only a few nanometers, e.g. in those abovementioned Ag-containing Mg-RE alloys [16–22]. The very small inter-precipitate distances of precipitates significantly hinder dislocation slip and deformation twinning, thus resulting in poor plasticity [23,24]. Consequently, replacing GBs and twin boundaries (TBs) with interfacial phases through controlled segregation was proposed to strengthen materials [25–27]. In recent years, interfacial phases have attracted extensive attention [28,29]. GBs and TBs have certain degrees of crystallographic disregistry [30,31], but phase transition as a combined result of interfacial energy reduction and solute segregation can restructure periodicity at GBs and/or TBs to form two-dimensional (2D) or three-dimensional (3D) interfacial phases [32].

The interfacial phase is confined at the interface between matrix grains, and has different structure and composition from the matrix [32–34]. For example, Ag segregation in a Mg-alloy led to the formation of a periodic spinal-shaped structure along the $\{10\bar{1}2\}_\alpha$ TBs and high-angle GBs [35]. It was also reported that interfacial phase plays an important role in tuning the microstructural characteristics and mechanical property [36–39]. However, there have been two major challenges in the research field of interfacial phases: First, it remains a challenge to determine the crystal strcutures of interfacial phases due to their limited thicknesses, which makes it difficult to observe them from three different crystal directions under eletron microscope; Second, local strain variation on an interface significantly affect the formation of interfacial phases, but such effect is not yet understood. In addition, while it is known that the nucleation and growth of precipitates in grain interior are very sensitive to temperature, the temperature sensitivity of interfacial phases is still unkown.

In this paper, we try to solve the first challenge by using an Mg-Gd-Y-Ag-Zr alloy as a model material for a comprehensive study on the formation mechanism of a novel interfacial phase formed at a high-angle grain boundary. For the first time, the 3D lattice structure of an interfacial phase and its orientation relationship with the matrix is determined using high-angle annular dark-field scanning transmission electron microscopy (HAADF-STEM) and Z contrast intensity analysis from three independent directions. Detailed analysis on the structures of grain boundaries and interfacial phases reveals that the formation of the interfacial phase is significantly affected by the atomic mismatch on the interface. In addition, we found that the thermal stability of the interfacial phase is much higher than the precipitates in grain interior. We produce an Mg-Gd-Y-Ag-Zr alloy having the nanoscale interfacial phase but without precipitated in grain interior, by controlled deformation and annealing. It is believed that interfacial phases are better for improving the combination of mechanical property and thermal stability than high density precipitates within grains [40–42]. This work points to a new route to process Mg alloys with outstanding mechanical properties.

2. Experimental methods

The alloy ingots were prepared by melting and mixing high purity Mg and Ag (99.95%) metals with Mg-30Zr and Mg-25RE (wt. %) (RE = Y and Gd) precursor alloys in an electric-resistant furnace under a mixed atmosphere of CO_2 and SF_6 with a volume ratio of 49:1. The detailed ingot casting procedure can be found in Ref. [43]. The composition of the alloy was determined as Mg-10.4Gd-1.6Y-2.0Ag-0.1Zr (wt. %) using an inductively coupled plasma atomic emission spectroscopy (ICP-AES) analyzer (Perkin-Elmer, Plasma 400). The as-cast ingots were solution treated at 500 °C for 12 h and quenched to room temperature in hot water. Samples with a dimension of $30 \times 20 \times 6$ mm^3 were used as the starting material for both cold rolling and hot rolling. Cold rolling was conducted at room temperature, and the sample cracked on the edges at 30% thickness reduction. On the other hand, samples for hot rolling were heated at 450 °C for 10 min before each rolling pass, and then rolled on a conventional hot roller with 0.1 mm thickness reduction per pass and total rolling reduction of 70%. Post-rolling annealing was performed at 250 °C, 300 °C, 350 °C, 400 °C and 450 °C. Each annealing was done for at least 30 min.

Transmission electron microscopy (TEM) specimens were cut from the rolling sheet and polished to a thickness of ~25 μm. Perforation by ion milling was carried out on a cold stage (−50 °C) with low angle (<3.5°) and low energy ion beam (<3 keV). Atomic-resolution high-angle annular dark-field (HAADF) observation was conducted in an aberration-corrected scanning transmission electron microscope (STEM) (FEI Titan G2) operated at 300 kV. 3D atomic structures were established using the software CrystalMaker. The symmetry of the proposed unit cell of the interfacial phase was analyzed using the simulation software Materials Studio 7.0. HAADF-STEM image simulations of interfacial phase were done using the software QSTEM. First-principles calculations were performed using the Vienna Ab initio Simulation Package (VASP) with the Perdew-Burk-Ernzerhof (PBE) generalized gradient approximation function [44].

3. Experimental results

Shown in Fig. 1 is a typical microstructure of the 70% hot rolled Mg-Gd-Y-Ag-Zr alloy. Pronounced lamellar structures were observed in grains. Previous investigations regarded them as deformation twins, which shall have specific orientation with respect to their parent grains [45]. In our material, three types of lamellar structures were identified by using selected area diffraction as shown in Fig. 1d, e and f. Two typical deformation twins, $\{10\bar{1}2\}_\alpha$ and $\{10\bar{1}1\}_\alpha$ twin, are found as shown in Fig. 1d and e, which have angles of ~86° and ~125° between the twin $\{0001\}_\alpha$ plane and the matrix $\{0001\}_\alpha$ plane as viewed from the $[11\bar{2}0]_\alpha$ zone axis, respectively. Additionally, there is another kind of lamellar structure that had a unique orientation relationship with the neighboring lamellar bands, as shown in Fig. 1f. The misorientation at the lamellar structure interface is 142°, which is not equal to any TB misorientation angle. Therefore, this type of lamellar structure is defined here as a lamellar band (LB) with a unique orientation relationship in which the two neighboring LBs share the same $[11\bar{2}0]_\alpha$ zone axis, the boundary between LBs is therefore named coaxial grain boundary (CGB). This kind of coaxial LBs is suitable for crystal structure analysis, because high-resolution TEM images at both sides of boundary can be obtained at the same time.

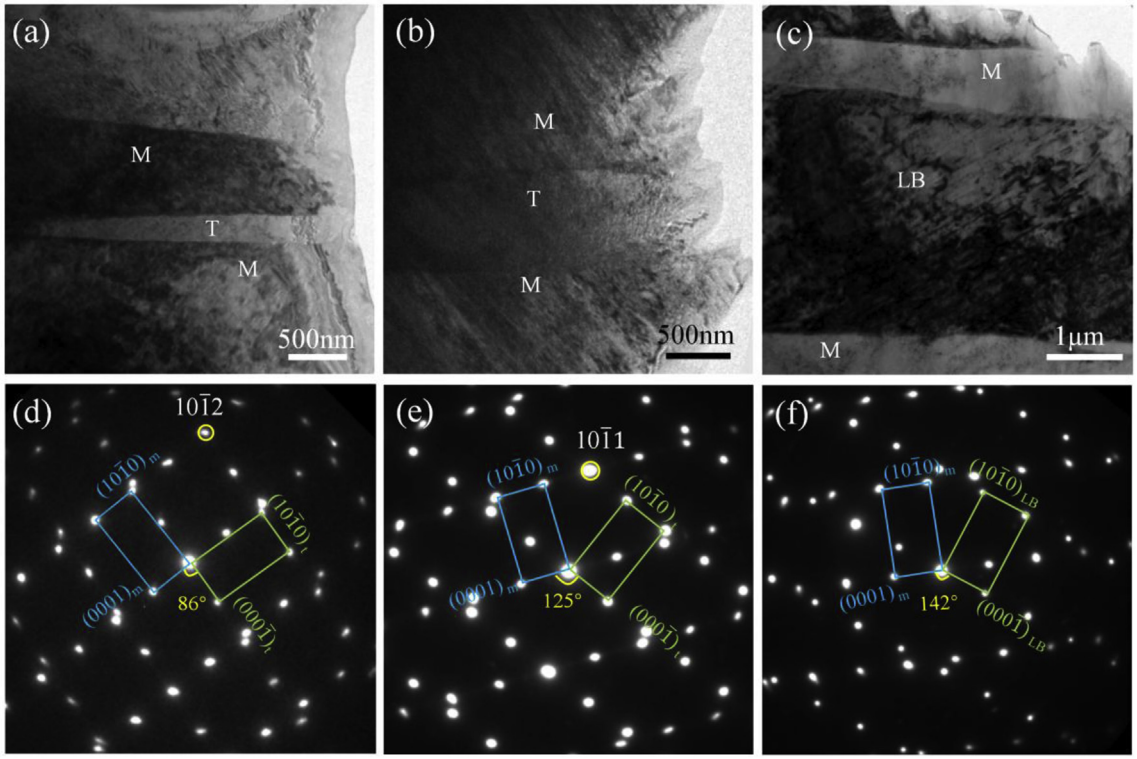

Fig. 1. TEM images in the hot rolled Mg-Gd-Y-Ag-Zr alloy: (a) $\{10\bar{1}2\}_\alpha$ twins; (b) $\{10\bar{1}1\}_\alpha$ twins; and (c) LB, and the corresponding selected area diffraction patterns (d), (e) and (f), respectively.

Due to strong segregation promoted by hot rolling, a very large number of solute atoms are concentrated at the CGBs to form the interfacial phase, as shown in Fig. 2a and b. The interfacial phase shown in Fig. 2a may be similar to the appearances of some conventional precipitates segregated at grain boundaries [46]. In classical nucleation theory, a newly formed precipitate will grow once it overcomes the nucleation barrier [47,48]. However, post annealing at temperatures up to 350 °C only improved the homogeneity and crystallinity of the interfacial phase, and the size/width of the interfacial phase shows no obvious growth (Fig. 2c, d, e, f, g and h). On the other hand, a high density of precipitates with sizes of a few tens of nanometers as marked in Fig. 2c are formed in the grain interior, after annealing at 250 °C and 300 °C for 30 min. According to the literature, the precipitates in grain interior are the β′ phase and γ'' phase [21,22,49]. Fig. 2g and h are the HAADF-STEM images of the sample annealed at 350 °C. While the interfacial phase is still stable, the β′ phase and γ'' phase in the grain interior have disappeared. This indicates that the interfacial phase has higher thermal stability than the β′ and γ'' phases. In addition, annealing at 400 °C and 450 °C was also carried out. The sample annealed at 400 °C exhibits the same morphology to the one annealed at 350 °C. However, when the annealing temperature was raised to 450 °C, significant recrystallization occurred, which led to grain refinement, defects recovery and dissolution of interfacial phase. Therefore, it is concluded that the interfacial phase is stable up to at least ~400 °C.

The observed interfacial phase is not viable outside of the CGB and TB regions, reflecting one of the important characteristics of complexions [42]. However, this interfacial structure has a 3D periodicity, which is different from complexions. Fig. 3a is an HAADF-STEM image showing some interfacial phase (marked with arrows) in the post annealed sample. The Z-contrast revealed many precipitates with heavier solute atoms (bright contrast) within the grain interior. Meanwhile, a large number of heavier solute atoms are also segregated to the GBs and formed the interfacial phase as marked by red, blue and green arrows; the marked regions of the interfacial phase are enlarged in Fig. 3b, c and d, respectively. In Fig. 3b, the interfacial phase has a unique ordered structure composing of multiple segments of periodic spinal-shaped structure. The structure of the interfacial phase looks similar to the segregated structure on the $\{10\bar{1}2\}_\alpha$ twin boundary [35] which has a spinal-shaped morphology. Fig. 3c and d indicate that the interfacial phase may expand to a larger area at a position with significant atomic distortion such as a triple junction. Fig. 3c corresponding to the blue arrow marked region in Fig. 3a is a triple junction where large stress concentration and atomic distortion is expected. Fig. 3d shows another big ledge, although this area is not a triple junction, the size of the interfacial phase is still larger than these commonly observed in Fig. 2. It is suspected that this big ledge was transformed from a residual primary $\{10\bar{1}2\}_\alpha$ twin. It will be discussed later that the strong strain field excreted from surrounding boundaries assisted the complete structural transition.

4. Discussion

4.1. Formation mechanism of the interfacial phase along the CGBs

In order to explore the nature of the interfacial phase formed along CGBs, detailed high-resolution transmission electron microscopy (HRTEM) analysis on the CGBs and surrounding structures have been conducted. A typical example is shown in Fig. 4a. The CGB located by an arrow in the image, has a thickness of a few atomic layers and creates a misorientation angle of 142°. Extensive HRTEM analysis (including Fig. 2b, d, f and h, Fig. 3b and d) reveals that along the CGB, there are many ledges of different sizes. Some big ledges such as the one shown in Fig. 3d are formed at the corner

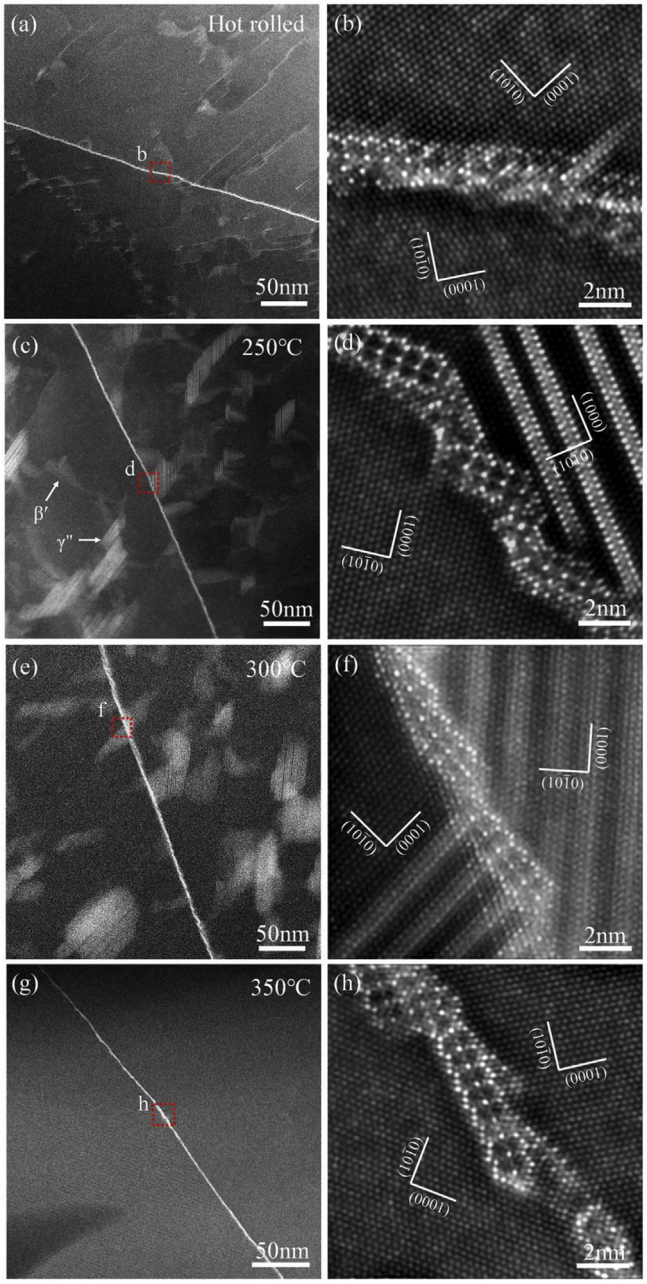

Fig. 2. HAADF-STEM images showing interfacial segregation at the CGBs in the hot rolled and post annealed Mg-Gd-Y-Ag-Zr alloy, obtained at the $[1\bar{2}10]_\alpha$ zone axis: (a), (c), (e) and (g) are high-resolution images of the hot rolled, sample annealed at 250 °C, 300 °C, 350 °C, respectively; (b), (d), (f) and (h) are atomic-resolution images of the truncated areas in (a), (c), (e) and (g), respectively.

adjacent to the $\{10\bar{1}2\}_\alpha$ and $\{10\bar{1}1\}_\alpha$ TBs, evidenced by the fact that both corners marked in Figs. 3d and 4a are ~19.5°. The "1st Twinning" region has a $\{10\bar{1}2\}_\alpha$ twin relationship with one side of the adjacent LB, and has a $\{10\bar{1}1\}_\alpha$ twin relationship with another side of the adjacent LB. Therefore, it is reasonable to propose that consecutive twinning in the same area has re-oriented a part of the grain twice to create the LB structure. As a result, the LB has a general misorientation of 142° with the matrix (Fig. 1f). Fig. 4b–d schematically illustrate the formation mechanism of the LB and the 142° CGB. Firstly, assuming that there is a grain that has the $[11\bar{2}0]_\alpha$ zone axis perpendicular to the page, and the basal plane is traced by a black line in Fig. 4b. When the grain is subjected to deformation, a primary $\{10\bar{1}2\}_\alpha$ twin forms. The $\{10\bar{1}2\}_\alpha$ twin is distinguished by blue atoms as shown in Fig. 4c. Further deformation leads to secondary $\{10\bar{1}1\}_\alpha$ twinning in the primary twin. Thus, the upper part of the grain marked by green atoms is re-oriented again by the secondary twinning. If secondary twinning reaches the primary twin boundary (TB), the primary TB can be distorted and transformed into a CGB which is marked by colored yellow in Fig. 4d. Meanwhile, many tiny residual parts of the primary $\{10\bar{1}2\}_\alpha$ twin are left along the CGB as large ledges (Fig. 3d). The residual "1st Twinning" part enclosed by the $\{10\bar{1}2\}_\alpha$ and $\{10\bar{1}1\}_\alpha$ TBs could be large as shown in Fig. 4a, then this region could be recognized as a new grain of a high aspect ratio (Fig. 4d, the blue region).

Fig. 4a is a HAADF-STEM image, therefore the Z-contrast is revealed. The bright atoms located along the GBs and TBs indicate strong segregation at the boundaries. This makes us wonder if the segregation and structuring are stress driven or thermal driven. In order to clarify this issue, the cold rolled samples to 30% thickness reduction are studied under HAADF-STEM observation. As shown in Fig. 5a, similar to conventional GBs, the 142° CGB in the cold rolled Mg-Gd-Y-Ag-Zr alloy are structurally incoherent, and the CGB contains much less solute atoms evidenced by less bright atoms than in Fig. 4a. Meshing is created in Fig. 5b (by connecting the atomic positions shown in Fig. 5a.) to reveal the degree of atomic distortions. This method is the Peak Pairs algorithm for strain mapping from HRTEM images carried out in Ref. [50]. Obviously, atomic mismatch is mainly along the CGB. In addition, significant atomic distortion is found in the truncated area in Fig. 5b and magnified in the insert. A $\{10\bar{1}2\}_\alpha$ TB is shown in Fig. 5c. Along the TB, there is no obvious lattice reconstruction nor solute atoms concentration, in comparison to Fig. 4a. Again atomic mismatch is mainly along the TB as shown in Fig. 5d. Therefore, it can be concluded here that the segregation and subsequent structuring of the interfacial phase found in the hot rolled samples (Figs. 2, 3 and 4) is strongly promoted by thermal energy input. Clearly, the formation of the interfacial phase along CGBs is energetically favorable. It lowers both the lattice strain and interfacial energy by having less vacancies and broken bonds than conventional GBs.

4.2. Composition and lattice structure of the interfacial phase

Based on the HAADF-STEM images from Figs. 3 and 4, schematics of the 2D lattice structures of the interfacial phase at the primary $\{10\bar{1}2\}_\alpha$ TBs and the CGBs are made in Fig. 6. The interfacial phase formed along a primary $\{10\bar{1}2\}_\alpha$ TB still possesses the twin relationship, but some of the atoms are replaced by heavier ones as shown in Fig. 4a. As schematically illustrated in Fig. 6a, the interfacial phase has a 2D symmetry with respect to the TB marked by the yellow arrow pair. Red spheres represent heavy atoms and blue spheres represent light atoms. For the interfacial phase formed along the 142° CGB (Figs. 3d and 6b), it shares some common feature with the TB phase that it has one half of the twin adjacent to the matrix side. On the other side, the atoms are rearranged into a new honeycomb structure as outlined by heavy atoms as shown in Fig. 6b.

The novel interfacial phase manifested at the interface and triple junction, as shown in Figs. 2, 3 and 4, is a result of phase transition process involving multilayer segregation and restructuring [42]. In order to achieve in-depth understanding of the specific interfacial phase structure, it is necessary to know the elements of the interfacial segregation. Fig. 7 shows the energy-dispersive X-ray spectroscopy (EDS) analysis of segregated elements of the Mg-Gd-Y-Ag-Zr alloy. Line scanning of EDS shows that the solute element enrichments of at the boundaries are mainly Gd and Ag, while the other two elements Y and Zr are hardly involved in interfacial segregation. Therefore, the high brightness of atomic columns in

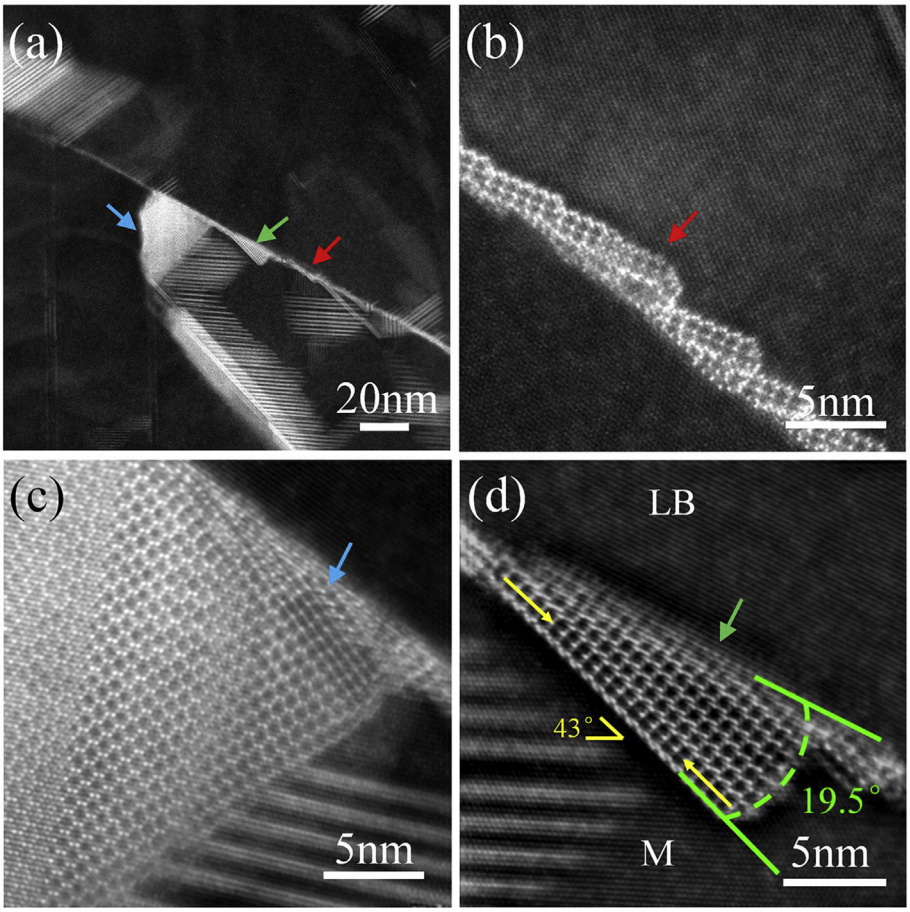

Fig. 3. HAADF-STEM images showing the interfacial phase in the Mg-Gd-Y-Ag-Zr alloy post annealed at 250 °C (obtained at the $[1\bar{2}10]_\alpha$ zone axis): (a) a high resolution image; (b), (c) and (d) are magnified views of the areas marked by red, blue and green arrows in (a), respectively. (For interpretation of the references to color in this figure legend, the reader is referred to the Web version of this article.)

the interfacial phase can be considered as Gd or Ag enriched columns. Shown in Fig. 7a, there are many parallel lines inside of the lamellar grain, which are probably dislocations or stacking faults segregated with solute atoms (linear complexions [33]). High resolution EDS mappings were carried out to analyze interfacial segregation (a very low voltage of 60 keV was used for noise reduction and radiation minimization) [51,52]. A typical result of the EDS analysis is illustrated in Fig. 8, which indicates that Y and Zr may be absent in the interfacial phase.

While segregation of Gd and Ag to TBs and GBs can be confirmed with EDS analysis (Figs. 7 and 8) and a corresponding literature [28], the tendency for segregation of Y and Zr to boundaries shall be checked by the aid of first-principles calculations. Thus, first-principles calculations were performed to estimate the segregation energy of Ag, Y, and Zr to $\{10\bar{1}2\}_\alpha$ TBs in the Mg matrix. The segregation energy is the difference in energy of a solute atom between occupying a boundary site and occupying a grain interior site. A supercell with 160 atoms (the model of supercell is provided in the supplemental Figure S1) was used in the calculation. The segregation energy at a $\{10\bar{1}2\}_\alpha$ twin ΔE_{seg} was calculated with the formula:

$$\Delta E_{seg} = \{[E_{twin}(Mg_{158}X_2) - E_{twin}(Mg_{160})] - [E_{bulk}(Mg_{158}X_2) - E_{bulk}(Mg_{160})]\} \quad (1)$$

Where $E_{twin}(Mg_{158}X_2)$ is the total energy of a supercell containing two segregated TBs. We used X to substitute one Mg atom in every TB (X = Ag, Y and Zr). $E_{twin}(Mg_{160})$ is the total energy of a pure Mg supercell containing two non-segregated TBs. $E_{bulk}(Mg_{158}X_2)$ is the total energy of a super-cell of Mg matrix, in which two segregated Mg atoms are also substituted by X. $E_{bulk}(Mg_{160})$ is the total energy of a pure Mg matrix supercell without any segregation.

As listed in Table 1, the Ag atom has a negative energy value, which indicates that Ag atoms are likely to segregate to $\{10\bar{1}2\}_\alpha$ TBs, complying with the EDS results (Figs. 7b and 8c). In contrast, the segregation energies of Y and Zr are positive, indicating that they are energetically unfavorable for segregation to TBs. Therefore, the tendency for segregation of Y and Zr to TBs are negligible. In current work, segregation have been found in both TBs and CGBs, it is widely accepted that TBs possess much lower energy than other types of GBs [53]. Therefore, the tendency for segregation to TBs shall be the same for other types of GBs including CGBs. Thus, this result complies with the experimental EDS result that Y and Zr are hardly found at TBs and CGBs. Therefore, only Gd, Ag and Mg will be considered with confidence in analyzing atomic occupancy in the interfacial phase structure.

Fig. 9a, c and e are the atomic-scale HAADF-STEM images of interfacial phase viewed at the $[11\bar{2}0]_\alpha$, $[0001]_\alpha$ and $[10\bar{1}0]_\alpha$ zone axes, respectively. The brightness of the spots (corresponding to columns of atoms) relates to the existence of atoms that are heavier than Mg within the columns of atoms, i.e. heavier atoms appear brighter. According to the EDS results in Figs. 7 and 8, the interfacial

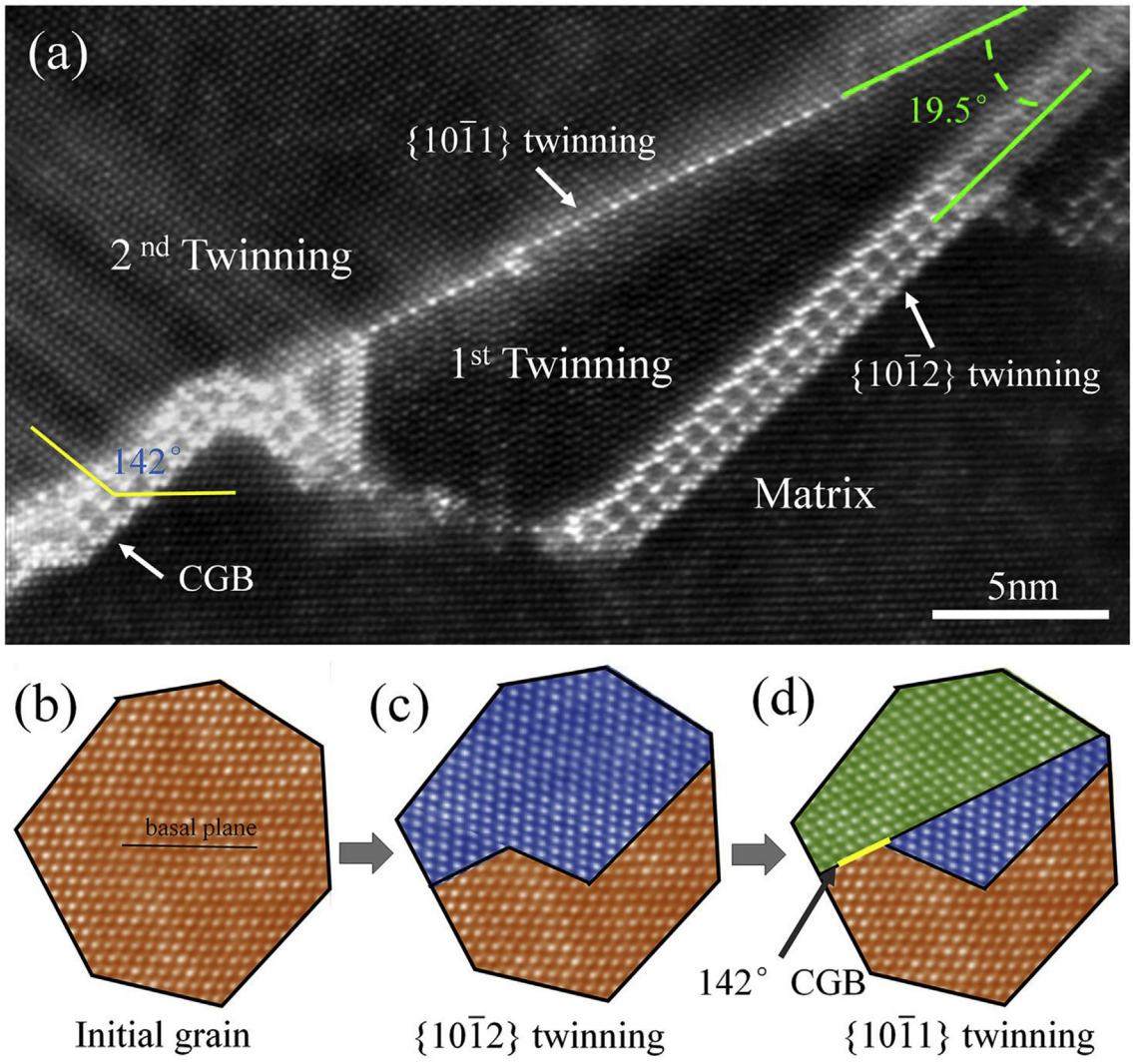

Fig. 4. Images of 142° CGB: (a) A HAADF-STEM image showing the correlation between the $\{10\bar{1}1\}_\alpha$ twin, $\{10\bar{1}2\}_\alpha$ twin and the 142° CGB (taken at the $[1\bar{2}10]_\alpha$ zone axis); (b), (c) and (d) schematically elucidate the formation process of the 142° CGB.

phase is composed of three elements, Gd, Ag and Mg. Careful analysis of the periodic intensities of the atomic columns from the HAADF-STEM images obtained at three different zone axes indicates that the atomic arrangements are periodic. As shown in Fig. 9, the periodicity of the atomic arrangement is short (one or two spots only) in all three directions and the variation of atomic brightness along each of the $[11\bar{2}0]_\alpha$, $[0001]_\alpha$ and $[10\bar{1}0]_\alpha$ directions is binary. Therefore, it is inferred that each column contains no more than two types of alloying elements, in a near 1:1 ratio. It is known that Gd (64)>Ag(47) in terms of atomic number, and both of them are larger than Mg(12). Gd has the highest atomic number among all possible elements in the alloy, thus the brightest columns should contain Gd atoms. The column contains only α-Mg matrix atoms should show the lowest Z-contrast. Magnified images and corresponding Z-contrast integrations of atomic columns are shown in Fig. 9b, d and f. The intensities of segregated atomic columns are compared to the benchmark brightness of α-Mg column which are marked by green arrows. In three different zone axes, atomic columns with four different levels of intensity that are brighter than the α-Mg column are observed. Four different intensity peaks are marked by red, purple, yellow and blue arrows. According to equation (2) [54], the intensity of atomic columns in a HAADF image is approximately proportional to the square of the atomic number Z.

$$\sigma_{(\theta)} = \frac{e^4 Z^2 d\Omega}{16(4\pi\varepsilon_0 E_0)^2 sin^4\ \frac{\theta}{2}} \tag{2}$$

where σ is scattering cross section, θ is scattering semi-angle, Ω is solid angle, e is electron charge, Z is atomic number, ε_0 is the dielectric constant and E_0 is energy of the electrons.

Table 2 lists five possible candidates of composition that may lead to the periodic undulation of brightness in HAADF-STEM images. It is initially proposed that the possible atomic columns are Gd rich column, Gd&Ag rich column, Gd&Mg rich column, Ag rich column, Ag&Mg rich columns and α-Mg rich column, and their brightness are in a descending order. The intensity values calculated by equation (2) indicate that the brightness of Gd&Mg rich column is very close to, but slightly higher than, the Ag rich column. The brightness of the two columns will be further discussed in conjunction with the experimental results later.

There are totally six column-compositions to match five intensity-levels. It is reasonable to deduce that the brightest atomic column I marked in Fig. 9d and f should be Gd rich column or

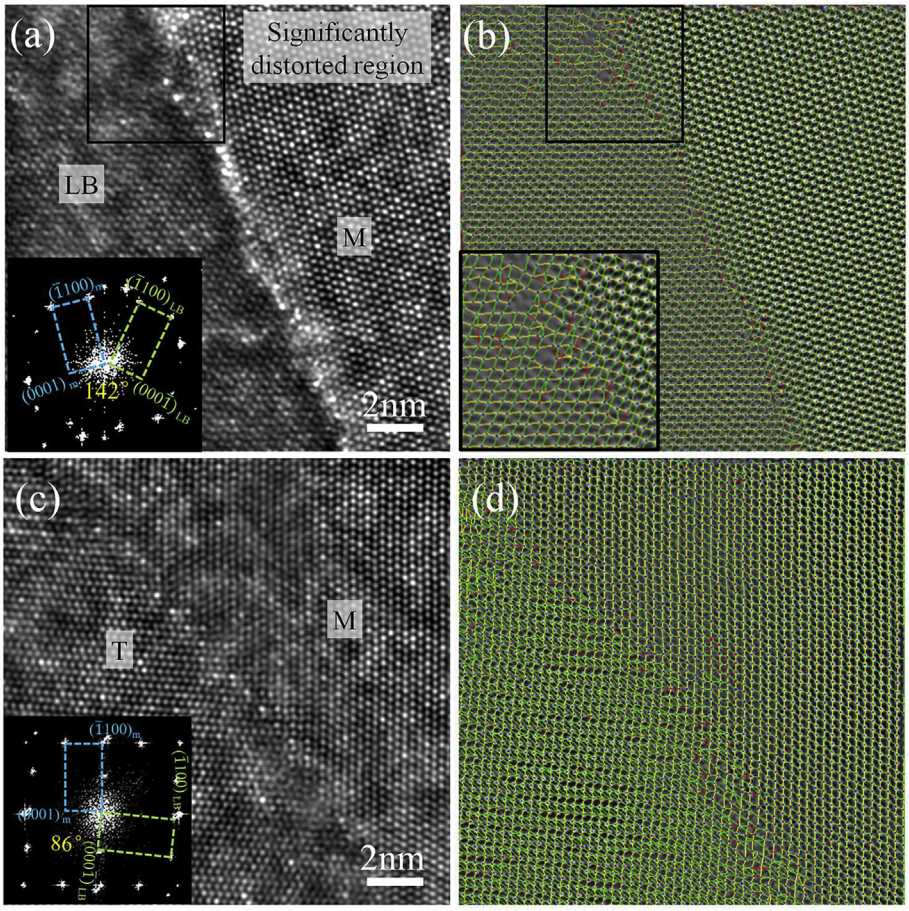

Fig. 5. Typical atomic structures of a 142° CGB and a $\{10\bar{1}2\}_\alpha$ TB in a cold rolled Mg-Gd-Y-Ag-Zr alloy: (a) a HAADF-STEM image and (b) a meshed image of a 142° CGB; (c) a HAADF-STEM image and (d) a meshed image of a $\{10\bar{1}2\}_\alpha$ TB.

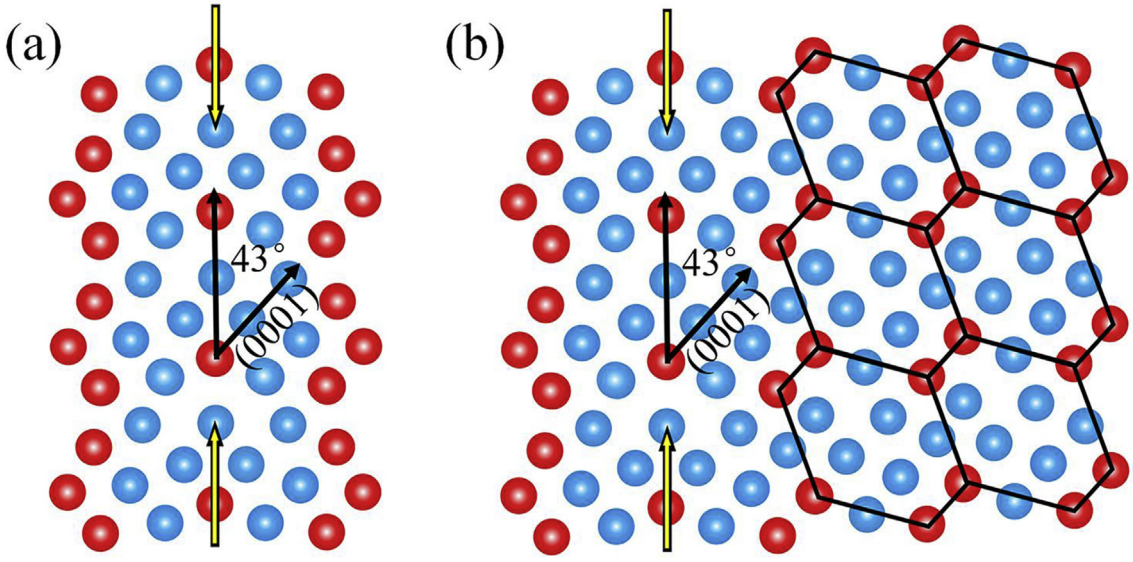

Fig. 6. Schematic illustrations of the 2D atomic arrangement of the interfacial phases along (a) the primary $\{10\bar{1}2\}_\alpha$ TB and (b) the 142° CGB.

Gd&Ag rich column; otherwise, there will not be enough choices of compositions to match the five intensity-levels. Meanwhile, Column I in Fig. 9d is parallel to the $[0001]_\alpha$ direction, which corresponds to the direction along the red dotted line in Fig. 9b. It is clearly that the red dotted line goes through spots with second lowest Z-contrast (blue arrows). The second lowest Z-contrast shall correspond to an Ag rich column or Ag&Mg rich column. Thus, the Column I parallel to the $[0001]_\alpha$ direction shall at least contain Ag or

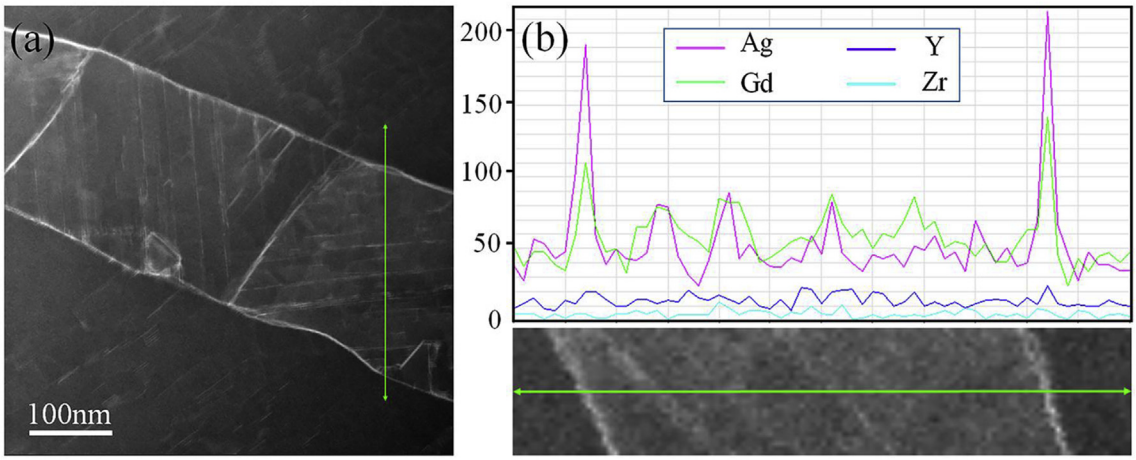

Fig. 7. EDS analysis of the interfacial segregation in the annealed Mg-Gd-Y-Ag-Zr alloy: (a) a HAADF-STEM image of a band structure enclosed by two 142° CGBs; (b) Line scanning EDS.

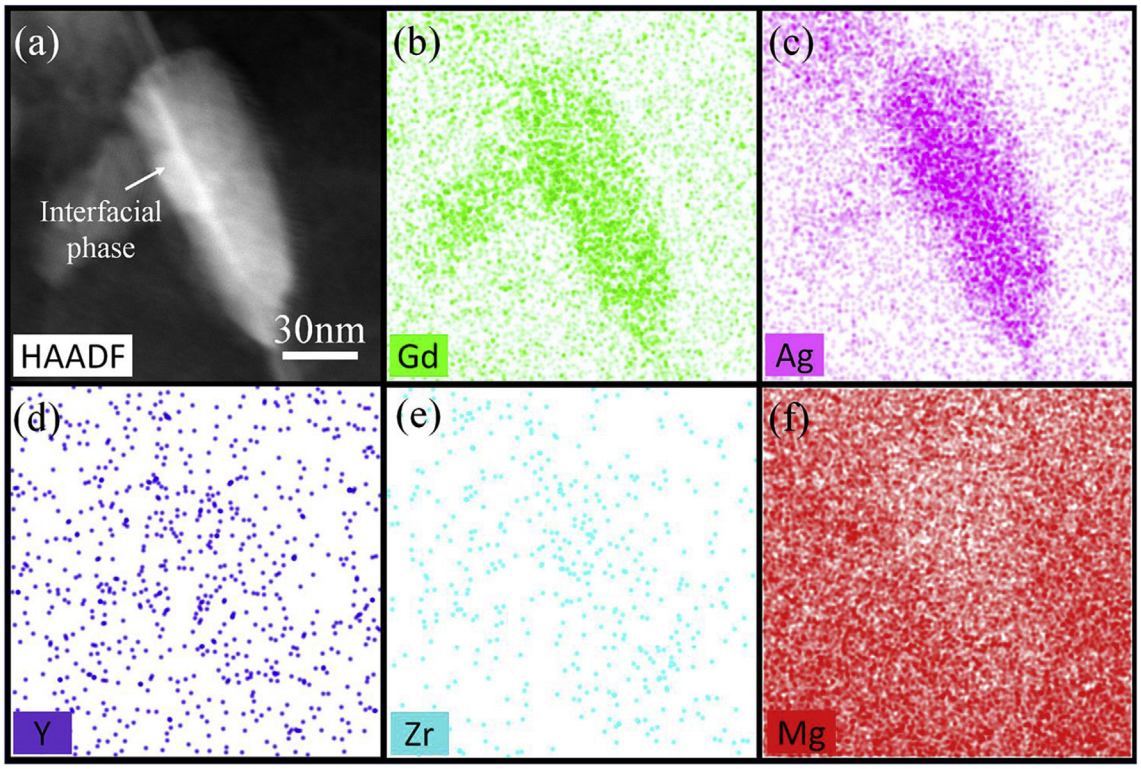

Fig. 8. EDS chemical mapping of the interfacial phase in the Mg-Gd-Y-Ag-Zr alloy: (a) the HAADF-STEM image and the corresponding (b) Gd-Kα; (c) Ag-Kα; (d) Y-Kα; (e) Zr-Kα; and (f) Mg-Kα distributions.

Table 1
Estimated segregation energies of Ag, Y and Zr atoms at $\{10\bar{1}2\}_\alpha$ twin boundaries.

$Mg_{158}Ag_2$	$Mg_{158}Y_2$	$Mg_{158}Zr_2$
−0.489 eV	0.146 eV	0.2445 eV

Mg. Since only Gd rich column or Gd&Ag rich column are possible, it can be deduced that Column I is the Gd&Ag rich column. Because the brightness from the Column I to the Column V is in a descending order, Candidate 5 in Table 2 shall be the correct choice of compositions. For candidate 5 in Table 2, Column II (purple) is determined as Gd&Mg rich column, and Column III (yellow) is the Ag rich column. As mentioned earlier, the brightness of Gd&Mg rich column is very close to the Ag rich column. In order to prevent observation errors, attention has been paid very carefully to Fig. 9b and d. Column II marked by a pink circle in Fig. 9b is parallel to the $[11\bar{2}0]_\alpha$ direction which corresponds to the direction along the blue dotted line in Fig. 9d. Column II can not be the Ag rich column, because the blue dotted line in Fig. 9d goes through an α-Mg rich column marked by a green circle. Therefore, the choice of Candidate 5 is justified by both calculation and experiment.

The elemental compositions in the atomic columns with different Z-contrast have been analyzed for $[11\bar{2}0]_\alpha$, $[0001]_\alpha$ and $[10\bar{1}0]_\alpha$ zone axes. 3D atomic model and corresponding projections

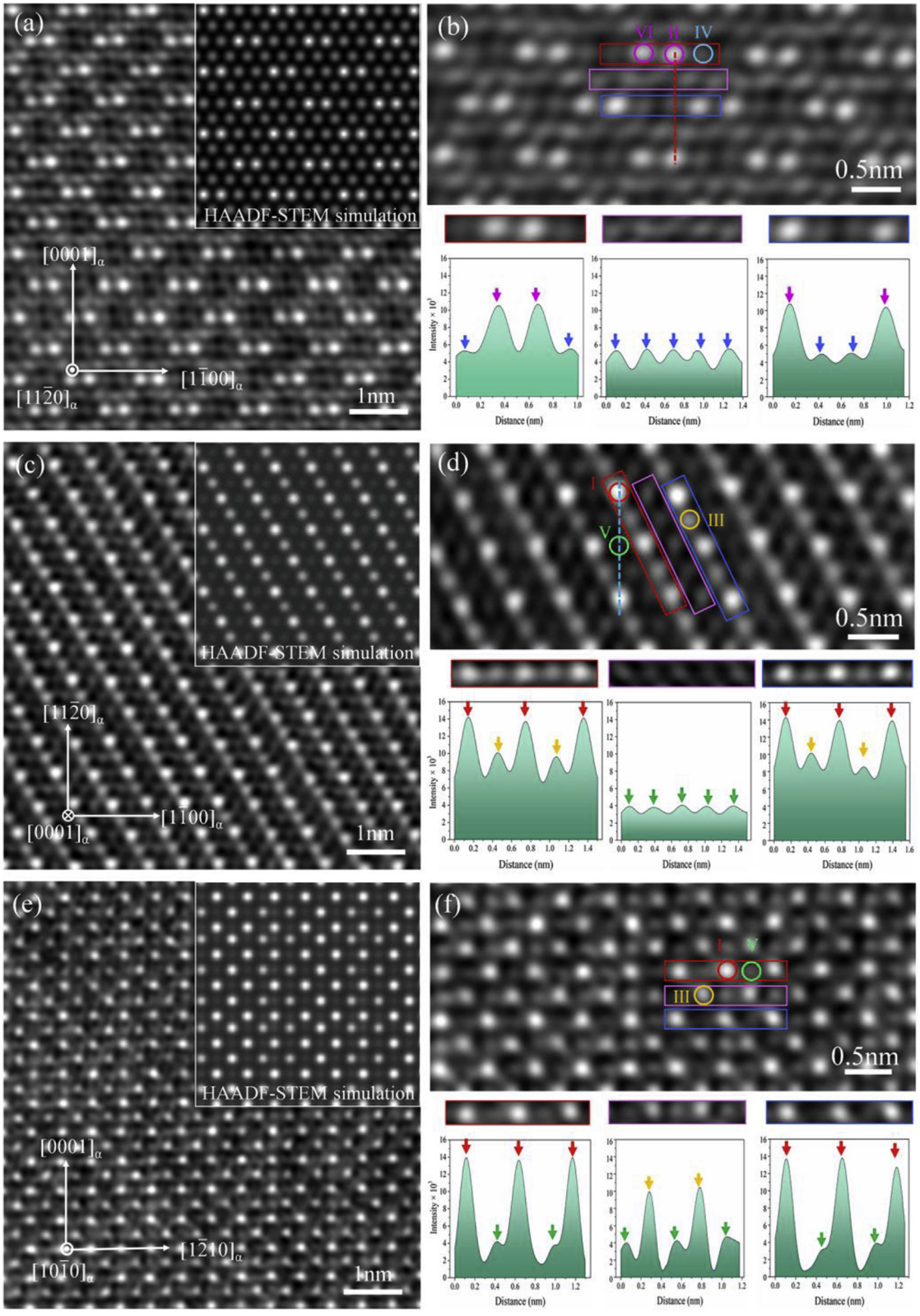

Fig. 9. Atomic resolution STEM images of the interfacial phase in the annealed Mg-Gd-Y-Ag-Zr alloy: (a) An HAADF-STEM image taken at the $[11\bar{2}0]_\alpha$ zone axis and (b) integration of the STEM intensity of the atomic columns; (c) an HAADF-STEM image taken at the $[0001]_\alpha$ zone axis and (d) integration of the STEM intensity of the atomic columns; and (e) an HAADF-STEM image taken at the $[10\bar{1}0]_\alpha$ zone axis and (f) integration of the STEM intensity of the atomic columns.

Table 2
Possible compositions of the bright atomic columns deduced from HAADF-STEM images taken at $[11\bar{2}0]_\alpha$, $[0001]_\alpha$ and $[10\bar{1}0]_\alpha$ zone axes.

Intensity	Candidate 1	Candidate 2	Candidate 3	Candidate 4	Candidate 5
I (red)	Gd	Gd	Gd	Gd	Gd&Ag
II (purple)	Gd&Ag	Gd&Ag	Gd&Ag	Gd&Mg	Gd&Mg
III (yellow)	Gd&Mg	Gd&Mg	Ag	Ag	Ag
IV (blue)	Ag	Ag&Mg	Ag&Mg	Ag&Mg	Ag&Mg
V (green)	α-Mg	α-Mg	α-Mg	α-Mg	α-Mg

in the three directions are established and shown in Fig. 10. Based on the crystal model in Fig. 10a, the HAADF-STEM simulation is performed (as inserted in Fig. 9a, c and e). The simulation shows a good agreement with the HAADF-STEM results in the $[11\bar{2}0]_\alpha$, $[0001]_\alpha$ and $[10\bar{1}0]_\alpha$ zone axes. The stacking order of atoms in some columns with the same Z-contrast is different, such as Column II and VI as shown in Figs. 9b and 10a. Thus, the symmetry of the unit cell of the interfacial phase is more complex than that shown in the HAADF-STEM images. Simulation software (Materials Studio 7) is employed to help resolve the symmetry and determine the space group. The space group of the 3D atomic model is determined to be *C2/m*. Fig. 10b–d shows the 2D models of interfacial phase in $[11\bar{2}0]_\alpha$, $[0001]_\alpha$ and $[10\bar{1}0]_\alpha$ zone axes, respectively. The atomic columns with the same composition but different atomic stacking orders are distinguished in Fig. 10b–d. Firstly, it is easy to find out the mirror symmetries in the projections of $[11\bar{2}0]_\alpha$ and $[10\bar{1}0]_\alpha$ zone axes (the symmetry planes are drawn in the figures) in Fig. 10b and d. However, there is no mirror symmetry in the projection of $[0001]_\alpha$ direction, in which only a twofold rotation axis is marked in Fig. 10c. It is known that both the $(11\bar{2}0)_\alpha$ and $(10\bar{1}0)_\alpha$ planes are perpendicular to $(0001)_\alpha$ plane. Based on the rules for the unit cell determination [55], the most possible unit cell of the interfacial phase should be a monoclinic structure. It is also verified by the Materials Studio 7 software.

From the above information, the 3D unit cell of the interfacial phase formed along CGBs is established and shown in Fig. 11a. The red, green and yellow spheres represent the Gd, Mg and Ag atoms, respectively, which are distributed in *C2/m* space group. Thus, the interfacial phase is proposed as a monoclinic structure with $\beta = 139.1°$, and its lattice parameters are $a = 1.20$ nm, $b = 1.04$ nm and $c = 1.59$ nm. The stoichiometry of interfacial phase is Mg_4GdAg_3. As shown in Fig. 11b, its orientation relationship with the Mg matrix is: $[101]//[11\bar{2}0]_\alpha$, $[302]//[10\bar{1}0]_\alpha$, and $(010)//(0001)_\alpha$.

Based on above results and analysis, it is concluded that Ag played an important role in the segregation and restructuring of the interfacial phase along the CGBs. The possible reasons are explained below. Firstly, the solubility of Ag in Mg decreases rapidly with decreasing temperature. In addition, the solubility of Ag in Mg is lower than 0.2% at 250 °C. Therefore, there is a large driving force for Ag to segregate to the interfaces. Secondly, the atomic radius of Ag is 0.144 nm, which is smaller than Mg (0.160 nm) and Gd (0.180 nm). It is easy for Ag to diffuse into interface and help with interfacial phase transition. Thirdly, if a small Ag atom and a large Gd atom pair up, their average radius is very close to that of the Mg matrix. Meanwhile, if an ordered structure is formed with

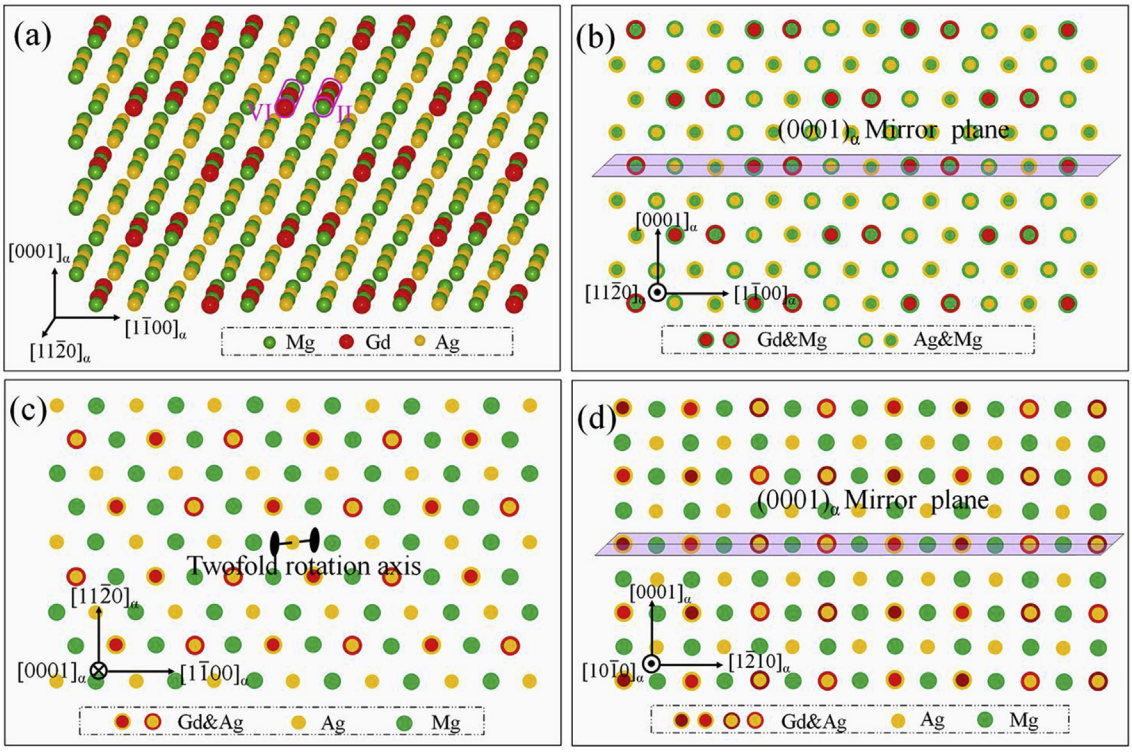

Fig. 10. Symmetry analysis of the proposed lattice of the interfacial phase: (a) a 3D atomic model of the interfacial phase, (b)–(d) 2D projections of the interfacial phase in $[11\bar{2}0]_\alpha$, $[0001]_\alpha$, and $[10\bar{1}0]_\alpha$ zone axes.

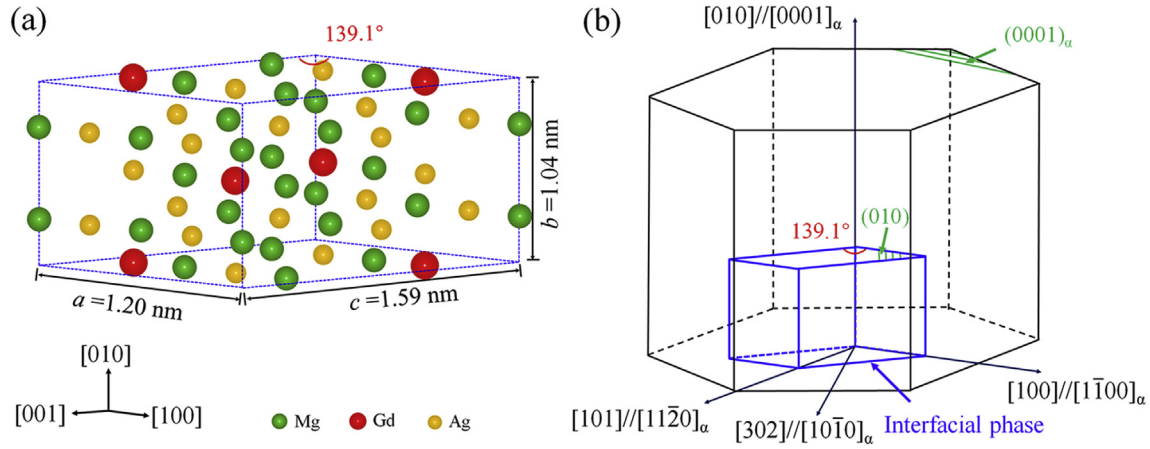

Fig. 11. The proposed crystal structure of the interfacial phase in Mg-Gd-Y-Ag-Zr alloy: (a) the proposed unit cell in which the red, green and yellow spheres represent the Gd, Mg and Ag atoms, respectively; (b) a schematic showing the orientation relationship between interfacial phase and the Mg matrix. (For interpretation of the references to color in this figure legend, the reader is referred to the Web version of this article.)

coordination of the Ag atoms and Gd atoms, the overall strain energy for the alloy system can be reduced. This may be the primary reason for the formation of the ordered interfacial phase observed along the CGBs. Fourthly, GB have high densities of defects that kinetically assist with the diffusion of alloy elements.

The comparatively low energy-state of the interfacial phase combined with the solute drag effect is beneficial for improving the thermal stability of the interfaces/CGBs at elevated temperatures up to 400 °C as shown in Fig. 2 [56,57]. The interfacial phase can effectively delay the dynamic recovery process and increase dislocation storage capacity by exerting strong pinning effect to the boundaries [56,58] and dislocations [33]. This is beneficial for sustaining high temperature strength of the material. However, the mechanical properties of the material are determined by three major microstructural features [30,59,60]: (1) boundaries including GBs and TBs, (2) precipitates and (3) solid solution. As shown in Fig. 2, the density of precipitates, the concentration of solute atoms in the matrix and the segregation at the boundaries are changing with temperature. It is difficult to deduce experimentally the sole effect of interfacial phase on mechanical properties. Thus, a comprehensive research with series of carefully designed experiments are required to explore the total benefit of the interfacial phase for mechanical properties of Mg-RE alloys.

5. Conclusions

A thermally stable interfacial phase formed uniformly along all 142° CGBs was found in a Mg-Gd-Y-Ag-Zr alloy. The formation mechanisms of the CGB formation and the subsequent interfacial phase were clarified. The crystal structure of the novel interfacial phase was unequivocally determined by HAADF-STEM and crystal modeling. The key findings are summarized as follows:

(1) The size of the interfacial phase is strictly confined by the size of the strain field along a CGB. The interfacial phase is formed to relieve shear stress and is more stable (up to 400 °C) than precipitates in grain interior

(2) Ag plays a critical role in the formation of the interfacial phase. Ag segregation to TBs leads to a unique structure with a spinal-shaped segment character. Ag segregation to the 142° CGB leads to an interfacial phase that expands from the spinal-shaped phase (primary $\{10\bar{1}2\}_\alpha$ TB). Pronounced Ag segregation is due to the small atomic radius of Ag. When the structure is ordered in coordination with large Gd atoms and small Ag atoms, the lattice strain and the number of vacancies can be reduced, leads to a lowered interfacial energy. The low energy nature of the CGB with the interfacial phase leads to higher stability.

(3) The interfacial phase formed along CGBs has a monoclinic ($\beta = 139.1°$) structure with a stoichiometry of Mg_4GdAg_3. Its lattice parameters are $a = 1.20$ nm, $b = 1.04$ nm, and $c = 1.59$ nm, and its space group is *C2/m*. Its orientation relationship with the Mg matrix is: $[101]//[11\bar{2}0]_\alpha$, $[302]//[10\bar{1}0]_\alpha$ and $(010)//(0001)_\alpha$.

Acknowledgements

The authors thank W. Guo, S. Pang and J.F. Liu for materials preparation, S.D. Sun for crystal modeling, and M.L. Sui and H.X. Sui for crystallography analysis. This work is supported by the National Key R&D Program of China (grant number 2017YFA0204403), the National Natural Science Foundation of China (grant numbers 51601003, 51601094, 51602155, 51074106), the Beijing Nova Program (grant number Z151100003150142), the Fok Ying-Tong Education Foundation of China (grant number 151006), and the Beijing Postdoctoral Research Foundation (grant number 2016ZZ-02).

Appendix A. Supplementary data

Supplementary data to this article can be found online at https://doi.org/10.1016/j.actamat.2018.10.005.

References

[1] B.C. Suh, M.S. Shim, K.S. Shin, N.J. Kim, Current issues in magnesium sheet alloys: where do we go from here? Scripta Mater. 84–85 (2014) 1–6.
[2] J.F. Nie, Precipitation and hardening in magnesium alloys, Metall. Mater. Trans. A 43 (2012) 3891–3939.
[3] T.M. Pollock, Weight loss with magnesium alloys, Science 328 (2010) 986–987.
[4] D. Wu, R.S. Chen, E.H. Han, Serrated flow and tensile properties of a Mg-Gd-Zn alloy, Mater. Sci. Eng., A 532 (2012) 267–274.
[5] L. Jiang, J.J. Jonas, A.A. Luo, A.K. Sachdev, S. Godet, Twinning-induced softening in polycrystalline AM30 Mg alloy at moderate temperatures, Scripta Mater. 54 (2006) 771–775.
[6] S.M. Zhu, M.A. Gibson, M.A. Easton, J.F. Nie, The relationship between microstructure and creep resistance in die-cast magnesium–rare earth alloys, Scripta Mater. 63 (2010) 698–703.
[7] H.R. Nodooshan, G.H. Wu, W.C. Liu, G.L. Wei, Y.L. Li, S. Zhang, Effect of Gd

content on high temperature mechanical properties of Mg-Gd-Y-Zr alloy, Mater. Sci. Eng., A 651 (2016) 840–847.
[8] T. Homma, N. Kunito, S. Kamado, Fabrication of extraordinary high strength magnesium alloy by extrusion, Scripta Mater. 61 (2009) 644–647.
[9] J.F. Nie, X. Gao, S.M. Zhu, Enhanced age hardening response and creep resistance of Mg-Gd alloys containing Zn, Scripta Mater. 53 (2005) 1049–1053.
[10] S.M. He, X.Q. Zeng, L.M. Peng, X. Gao, J.F. Nie, W.J. Ding, Microstructure and strengthening mechanism of high strength Mg-10Gd-2Y-0.5Zr alloy, J. Alloy. Comp. 427 (2007) 316–323.
[11] Z.L. Ning, J.Y. Yi, M. Qian, H.C. Sun, F.Y. Cao, H.H. Liu, J.F. Sun, Microstructure and elevated temperature mechanical and creep properties of Mg-4Y-3Nd-0.5Zr alloy in the product form of a large structural casting, Mater. Des. 60 (2014) 218–225.
[12] G.R. Ebrahimi, A.R. Maldar, H. Monajati, M. Haghshenas, Hot deformation behavior of AZ91 magnesium alloy in temperature ranging from 350 °C to 425 °C, Trans. Nonferrous Metals Soc. China 22 (2012) 2066–2071.
[13] K. Hantzsche, J. Bohlen, J. Wendt, K.U. Kainer, S.B. Yi, D. Letzig, Effect of rare earth additions on microstructure and texture development of magnesium alloy sheets, Scripta Mater. 63 (2010) 725–730.
[14] L.L. Tang, Y.H. Zhao, R.K. Islamgaliev, R.Z. Valiev, Y.T. Zhu, Microstructure and thermal stability of nanocrystalline Mg-Gd-Y-Zr alloy processed by high pressure torsion, J. Alloy. Comp. 721 (2017) 577–585.
[15] B.Z. Wang, C.M. Liu, Y.H. Gao, S.N. Jiang, Z.Y. Chen, Z. Luo, Microstructure evolution and mechanical properties of Mg-Gd-Y-Ag-Zr alloy fabricated by multidirectional forging and ageing treatment, Mater. Sci. Eng., A 702 (2017) 22–28.
[16] Q.D. Wang, J. Chen, Z. Zhao, S.M. He, Microstructure and super high strength of cast Mg-8.5Gd-2.3Y-1.8Ag-0.4Zr alloy, Mater. Sci. Eng., A 528 (2010) 323–328.
[17] Y. Zhang, Y.J. Wu, L.M. Peng, P.H. Fu, F. Huang, W.J. Ding, Microstructure evolution and mechanical properties of an ultra-high strength casting Mg-15.6Gd-1.8Ag-0.4Zr alloy, J. Alloy. Comp. 615 (2014) 703–711.
[18] W.W. Jian, G.M. Cheng, W.Z. Xu, C.C. Koch, Q.D. Wang, Y.T. Zhu, S.N. Mathaudhu, Physics and model of strengthening by parallel stacking faults, Appl. Phys. Lett. 103 (2013) 133108.
[19] W.W. Jian, G.M. Cheng, W.Z. Xu, H. Yuan, M.H. Tsaia, Q.D. Wang, C.C. Koch, Y.T. Zhu, S.N. Mathaudhu, Ultrastrong Mg alloy via nano-spaced stacking faults, Mater. Res. Lett. 1 (2013) 61–66.
[20] K. Yamada, H. Hoshikawa, S. Maki, T. Ozaki, Y. Kuroki, S. Kamado, Y. Kojima, Enhanced age-hardening and formation of plate precipitates in Mg-Gd-Ag alloys, Scripta Mater. 61 (2009) 636–639.
[21] Y.M. Zhu, A.J. Morton, J.F. Nie, Characterisation of intermetallic phases in an Mg-Y-Ag-Zn casting alloy, Phil. Mag. Lett. 90 (2010) 173–181.
[22] Y.M. Zhu, K. Oh-Ishi, N.C. Wilson, K. Hono, A.J. Morton, J.F. Nie, Precipitation in a Ag-Containing Mg-Y-Zn alloy, Metall. Mater. Trans. 47 (2016) 927–940.
[23] Z.J. Yu, C. Xu, J. Meng, S. Kamado, Microstructure evolution and mechnical properties of a high strength Mg-11.7Gd-4.9Y-0.3Zr (wt.%) alloy propared by predeformation annealing, hot extrusion and ageing, Mater. Sci. Eng., A 703 (2017) 348–358.
[24] J.J. Bhattacharyya, F. Wang, P.J. McQuade, S.R. Agnew, Deformation and fracture behavior of Mg alloy, WE43, after various aging heat treatment, Mater. Sci. Eng. 705 (2017) 79–88.
[25] N.B. Tork, S.H. Razavi, H. Saghafian, R. Mahmudi, Microstructural evolution and mechnical properties of the as-cast and extruded Mg-Gd alloys, Adv. Eng. Mater. 18 (2016) 156–161.
[26] H. Somekawa, H. Watanabe, D.A. Basha, A. Singh, T. Inoue, Effect of twin boundary segregation on damping properties in magnesium alloy, Scripta Mater. 129 (2017) 35–38.
[27] P.V. Liddicoat, X.Z. Liao, Y.H. Zhao, Y.T. Zhu, M.Y. Murashkin, E.J. Lavernia, R.Z. Valiev, S.P. Ringer, Nanostructural hierarchy increases the strength of aluminium alloys, Nat. Commun. 1 (2010) 63.
[28] J.F. Nie, Y.M. Zhu, J.Z. Liu, X.Y. Fang, Periodic segregation of solute atoms in fully coherent twin boundaries, Science 340 (2013) 957–960.
[29] D.A. Basha, R. Sahara, H. Somekawa, J.M. Rosalie, A. Singh, K. Tsuchiya, Interfacial segregation induced by severe plastic deformation in a Mg-Zn-Y alloy, Scripta Mater. 124 (2016) 169–173.
[30] J.P. Buban, K. Matsunaga, J. Chen, N. Shibata, W.Y. Ching, T. Yamamoto, Y. Ikuhara, Grain boundary strengthening in alumina by rare earth impurities, Science 311 (2006) 212–215.
[31] Z.C. Wang, M. Saito, K.P. McKenna, L. Gu, S. Tsukimoto, A.L. Shluger, Y. Ikuhara, Atom-resolved imaging of ordered defect superstructures at individual grain boundaries, Nature 479 (2011) 380–383.
[32] S.J. Dillon, M. Tang, W.C. Carter, M.P. Harmer, Complexion: a new concept for kinetic engineering in materials science, Acta Mater. 55 (2007) 6208–6218.
[33] M. Kuzmina, M. Herbig, D. Ponge, S. Sandlobes, D. Raabe, Linear complexions: confined chemical and structural states at dislocations, Science 349 (2015) 1080–1083.
[34] A.L. Chua, N.A. Benedek, L. Chen, M.W. Finnis, A.P. Sutton, A genetic algorithm for predicting the structures of interfaces in multicomponent systems, Nat. Mater. 9 (2010) 418–422.
[35] H. Zhou, G.M. Cheng, X.L. Ma, W.Z. Xu, S.N. Mathaudhu, Q.D. Wang, Y.T. Zhu, Effect of Ag oninterfacial segregation in Mg-Gd-Y-(Ag)-Zr alloy, Acta Mater. 95 (2015) 20–29.
[36] N. Stanford, G. Sha, J.H. Xia, S.P. Ringer, M.R. Barnett, Solute segregation and texture modification in an extruded magnesium alloy containing gadolinium, Scripta Mater. 65 (2011) 919–921.
[37] Y.X. Li, J. Wang, K.G. Chen, M.Y. Shao, Y. Shen, L. Jin, G.Z. Zhu, Self-patterning Gd nano-fibers in Mg-Gd alloys, Sci. Rep. 6 (2016) 38537.
[38] J.D. Robson, Effect of rare-earth additions on the texture of wrought magnesium alloys: the role of grain boundary segregation, Metall. Mater. Trans. A 45 (2014) 3205–3212.
[39] M. Bugnet, A. Kula, M. Niewczas, G.A. Botton, Segregation and clustering of solutes at grain boundaries in Mg-rare earth solid solutions, Acta Mater. 79 (2014) 66–73.
[40] R. Kirchheim, Grain coarsening inhibited by solute segregation, Acta Mater. 50 (2002) 413–419.
[41] S.C. Pun, W.B. Wang, A. Khalajhedayati, J.D. Schuler, J.R. Trelewicz, T.J. Rupert, Nanocrystalline Al-Mg with extreme strength due to grain boundary doping, Mater. Sci. Eng., A 696 (2017) 400–406.
[42] P.R. Cantwell, M. Tang, S.J. Dillon, J. Luo, G.S. Pohrer, M.P. Harmer, Grain boundary complexions, Acta Mater. 62 (2014) 1–48.
[43] H. Zhou, Q. Wang, J. Chen, B. Ye, W. Guo, Trans. Microstructure and mechanical properties of extruded Mg-8.5Gd-2.3Y-1.8Ag-0.4Zr alloy, Nonferrous Metals Soc 22 (2012) 1891–1895.
[44] Y.F. Wu, S. Li, Z.G. Ding, W. Liu, Y.H. Zhao, Y.T. Zhu, Effects of charge redistribution factor F on stacking-fault energies of Mg-based binary alloys, Scripta Mater. 112 (2016) 101–105.
[45] K.H. Kim, B.C. Suh, J.H. Bae, M.S. Shim, S. Kim, N.J. Kim, Microstructure and texture evolution of Mg alloys during twin-roll casting and subsequent hot rolling, Scripta Mater. 63 (2010) 716–720.
[46] Y.H. Zhao, X.Z. Liao, Z. Jin, R.Z. Valiev, Y.T. Zhu, Microstructure and mechanical properties of ultrafine grained 7075 Al alloy processed by ECAP and their evolutions during annealing, Acta Mater. 52 (2004) 4589–4599.
[47] J.W. Oxtoby, Homogeneous nucleation: theory and experiment, J. Phys. Condens. Matter 4 (1992) 7627–7650.
[48] T. Palberg, Crystallization kinetics of repulsive colloidal spheres, J. Phys. Condens. Matter 11 (1999) 323–360.
[49] Y. Zhang, Y.M. Zhu, W. Rong, Y.J. Wu, L.M. Peng, J.F. Nie, N. Birbilis, On the precipitation in an Ag-containing Mg-Gd-Zr alloy, Metall. Mater. Trans. A 49 (2018) 673–694.
[50] P.L. Galindo, S. Kret, A.M. Sanchez, J.Y. Laval, A. Yáñez, J. Pizarro, E. Guerrero, T. Ben, S.I. Molina, The peak pairs algorithm for strain mapping from HRTEM images, Ultromicroscopy 107 (2007) 1186–1193.
[51] W.Z. Xu, Y.F. Zhang, G.M. Cheng, W.W. Jian, P.C. Millett, C.C. Koch, S.N. Mathaudhu, Y.T. Zhu, In-situ atomic-scale observation of irradiation-induced void formation, Nat. Commun. 4 (2013) 2288.
[52] W.Z. Xu, Y.F. Zhang, G.M. Cheng, W.W. Jian, P.C. Millett, C.C. Koch, S.N. Mathaudhud, Y.T. Zhu, Dynamic void growth and shrinkage in Mg under electron irradiation, Mater. Res. Lett. 2 (2014) 176–183.
[53] Y. Cao, S. Ni, X.Z. Liao, M. Song, Y.T. Zhu, Structural evolutions of metallic materials processed by severe plastic deformation, Mater. Sci. Eng. R 133 (2018) 1–59.
[54] D.B. Williams, C.B. Carter, Transmission Electron Microscopy: a Textbook for Materials Science, second ed., Springer, 2009, p. 760.
[55] V.K. Pecharsky, P.Y. Zavalij, Fundamental of Power Diffraction and Structural Characterization of Materials, second ed., Spring, 2009, p. 741.
[56] Y.J. Lin, H.M. Wen, Y. Li, B. Wen, W. Liu, E. Lavernia, An analytical model for stress-induced grain growth in the presence of both second-phase particles and solute segregation at grain boundaries, Acta Mater. 82 (2015) 304–315.
[57] Y. Chen, N. Gao, G. Sha, S.P. Ringer, M.J. Starink, Strengthening of an Al-Cu-Mg alloy processed by high-pressure torsion due to clusters, defects and defect-cluster complexes, Mater. Sci. Eng., A 627 (2015) 10–20.
[58] L.H. Wang, X.D. Han, P. Liu, Y.H. Yue, Z. Zhang, E. Ma, In situ observation of dislocation behavior in nanometer grains, Phys. Rev. Lett. 105 (2010) 135501.
[59] J.H. Chen, E. Costan, M.A. van Huis, Q. Xu, H.W. Zandbergen, Atomic pillar-based nanoprecipitates strengthen AlMgSi alloys, Science 312 (2006) 416–419.
[60] C.H. Liu, X.L. Li, S.H. Wang, J.H. Chen, Q. Teng, J. Chen, A tuning nano-precipitation approach for achieving enhanced strength and good ductility in Al alloys, Mater. Des. 54 (2014) 144–148.